Journal of Magnetic Resonance 212 (2011) 440–449

Contents lists available at SciVerse ScienceDirect

Journal of Magnetic Resonance

journal homepage: www.elsevier.com/locate/jmr

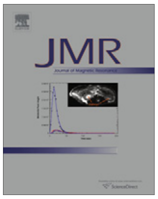

THz-waves channeling in a monolithic saddle-coil for Dynamic Nuclear Polarization enhanced NMR

A. Macor [a,b,*], E. de Rijk [a,b], G. Annino [c], S. Alberti [d], J.-Ph. Ansermet [a]

[a] Institut de Physique de la Matire Condense, Ecole Polytechnique Fédérale de Lausanne, Station 3, CH-1015 Lausanne, Switzerland
[b] SWISS to 12 Sàrl, 1015 Lausanne, Switzerland
[c] Istituto per i Processi Chimico-Fisici, CNR-IPCF, via G. Moruzzi 1, Pisa, Italy
[d] Centre de Recherche en Physique des Plasmas, Ecole Polytechnique Fédérale de Lausanne, Station 13, CH-1015 Lausanne, Switzerland

ARTICLE INFO

Article history:
Received 20 May 2011
Revised 21 July 2011
Available online 24 August 2011

Keywords:
Nuclear Magnetic Resonance (NMR)
Dynamic Nuclear Polarization (DNP)
THz waves
Radio-frequencies
Millimeter waves
Non-resonant cavities
Probe-head

ABSTRACT

A saddle coil manufactured by electric discharge machining (EDM) from a solid piece of copper has recently been realized at EPFL for Dynamic Nuclear Polarization enhanced Nuclear Magnetic Resonance experiments (DNP-NMR) at 9.4 T. The corresponding electromagnetic behavior of radio-frequency (400 MHz) and THz (263 GHz) waves were studied by numerical simulation in various measurement configurations. Moreover, we present an experimental method by which the results of the THz-wave numerical modeling are validated. On the basis of the good agreement between numerical and experimental results, we conducted by numerical simulation a systematic analysis on the influence of the coil geometry and of the sample properties on the THz-wave field, which is crucial in view of the optimization of DNP-NMR in solids.

1. Introduction

Transferring the high polarization of electron spins to the less polarized nuclear spins is at the basis of DNP techniques, which is emerging as an extremely powerful approach to increase the sensitivity of NMR [1–9].

DNP can cover a broad range of applications, including NMR on solids, liquids or surfaces, solely requiring the presence of a paramagnetic species in the sample. DNP-NMR techniques have been investigated since the 50s both theoretically and experimentally. These studies were conducted mainly at low magnetic fields [10–12], with notable exceptions [13–15]. It is only in the last two decades that these techniques have drawn important interest, owing to the studies of the polarization mechanisms [16] and to new instrumental achievements. The development of cyclotron resonance masers (gyrotrons) as THz-wave sources with output power and spectral purity suited for DNP NMR, lead to the seminal work by Griffin and co-workers in the early 90s on DNP NMR of solids with magic angle spinning. These results demonstrated about two orders of magnitude signal enhancement, corresponding to a reduction in the acquisition time of about four orders of magnitude or, at a fixed acquisition time and signal-to-noise, to a reduction of two orders of magnitude in the size of sample [17,18] . Alternatively, DNP enhancement can be used to reduce the acquisition time of multi-dimensional spectra [19].

In parallel to the development of efficient THz-wave sources, consistent efforts have been dedicated to the development of innovative probe-heads, capable to establish the state-of-the-art in their radio-frequency (RF) and microwave (THz) performances, mainly in the current-to-magnetic field conversion factor for the radio-frequency part [20], and power-to-magnetic field conversion factor, for the microwave part [21]. Since an efficient DNP polarization is expected for an intense microwave irradiation of the sample, a typical problem related to this technique is given by the possible microwave heating. This issue is of crucial importance in the case of liquid-state NMR, where the DNP enhancement effect is determined by the Overhauser effect [10,11]. According to the common theoretical models [12], the liquid-state DNP enhancement, ϵ, is provided by

$$\epsilon = \left|\frac{\gamma_e}{\gamma_n}\right| \cdot \xi \cdot f \cdot s \tag{1}$$

where $\gamma_e = -28.02$ GHz/T (resp. $\gamma_n = 42.6$ MHz/T) is the free electron gyromagnetic ratio (resp. nuclear), ξ is the coupling factor that describes the magnetization transfer (cross relaxation) from the electron to the nuclear spin, f is the leakage factor representing the paramagnetic enhancement to the nuclear relaxation rate over the

---

* Corresponding author.
E-mail address: alessandro.macor@epfl.ch (A. Macor).

1090-7807/$ - see front matter
doi:10.1016/j.jmr.2011.08.022

total nuclear relaxation rate, and s the saturation factor that represents the saturation of the electron Zeeman transitions. Assuming that the leakage factor and the saturation factor are relatively close to unity, as typical in the most advances experimental conditions, the efficiency of the nuclear polarization is related to the coupling factor, which in turn is strongly dependent on the temperature of the sample [22,23]. At high T, the DNP enhancement can deteriorate [23]. Moreover, a significant increase in the sample temperature is in any case detrimental for biological samples, where it induces denaturation. The fact that biological samples are characterized by high dielectric losses motivates the importance of a very well controlled THz-field distribution in the sample region. Moreover, the constraints related to DNP add to those typical of pulsed NMR techniques. Among them, it is worthwhile to mention the homogeneity of the RF magnetic field, B_{RF}. The importance of this homogeneity can be understood considering the nutation angle, Θ, imposed by the RF on the nuclear magnetization, given by:

$$\Theta = 2\pi \cdot B_{RF} \cdot \gamma_n \cdot \tau \qquad (2)$$

where γ is the gyromagnetic ratio of the considered nucleus, and τ is the pulse duration. An inhomogeneous magnetic field B_{RF} inside the sample volume implies that not every spin gets the same tip angle, which means that after few or long pulses, as those required in the most advanced spin sequences or in 2D studies, the magnetization is scrambled and consequently the signal-to-noise ratio decreases.

When designing a general purpose DNP NMR probe, the above technical constraints can be summarized in: high radio-frequency current-to-magnetic field conversion factor, high THz-wave power-to-magnetic field conversion factor, and high spatial homogeneity of radio-frequency magnetic fields inside the sample volume. Moreover, a high homogeneity is also desirable for the THz magnetic field, B_{THz}, since this ensures a homogeneous DNP enhancement. Finally, the THz-wave propagation circuit should have moderate propagation losses, in order to exploit the power delivered by the source. Keeping this in mind, in this work we investigated the performance of a in-house designed monolithic saddle coil designed for a 400 MHz NMR spectrometer. The magnetic field of the NMR spectrometer being 9.4 T imposes the THz frequency as 263 GHz. The geometry of the coil [24], shown in Fig. 1a and b, seems suitable for the injection of the THZ-beam coaxially into the sample, an option that was recently used [25]. In particular, here we study the details of the propagation of a THz wave through the saddle coil for DNP-NMR purposes in solid samples. The simulations are compared with experimental data taken with a coil manufactured by electric discharge machining. The simulations also provide the radio-frequency magnetic field produced by a current injected into the saddle coil. All the simulations presented in this work have been run with *Multiphysics* 3.5*a* (Comsol, SE), which is a finite-element analysis software environment for the modeling and simulation of coupled physical and chemical problems. Since the simulated volume is strongly over-moded, *i.e.* is significantly larger than the wavelength in free space (~1.14 mm at 263 GHz), this implies a very large number of meshing points for an accurate modeling. For this reason simulations have been run on a work station equipped with 144 GByte of RAM. This paper is organized as follows: Section 2 describes the numerical work done to evaluate the homogeneity and the time RMS intensity of the magnetic field at 400 MHz used for NMR. Section 3 introduces the experimental framework we developed to validate the numerical simulations at 263 GHz. The results are shown and commented in Section 4. We conclude and suggest some perspective in the last section.

2. Radio-frequency results

The saddle coil design proposed in this work, shown in Fig. 1a, is inspired by previous self standing coils [26,27], while being adapted to be compatible with standard liquid NMR test tubes and to our 9.4 T spectrometer. A high, continuous, and controlled electric conductivity through the structure, as well as a good mechanical stability, can be obtained by manufacturing the coil from a single solid piece of conductor, for instance by wire Electrical Discharge Machining (EDM). The obtained monolithic coil is not prone to the imperfections due to the soldering in the sample region. As can be seen in Fig. 1, the proposed Saddle coil has two connectors that point out perpendicularly to the axis of its cylindrical geometry. These connectors can be soldered to a standard NMR tuning and matching circuit in order to adjust its impedance at 400 MHz to the one of the NMR spectrometer. The impedance of the proposed saddle coil prototype alone was measured to be 58 nH at 400 MHz by using a network analyzer.

Saddle coils are widely used for NMR measurements and extensive research has been performed in order to optimize the radio-frequency magnetic field homogeneity over the sample region [27].

In particular, a possible, idealized monolithic saddle-coil geometry consists of a tube from which two diametrically opposite windows covering around 120° are removed. The proposed saddle coil

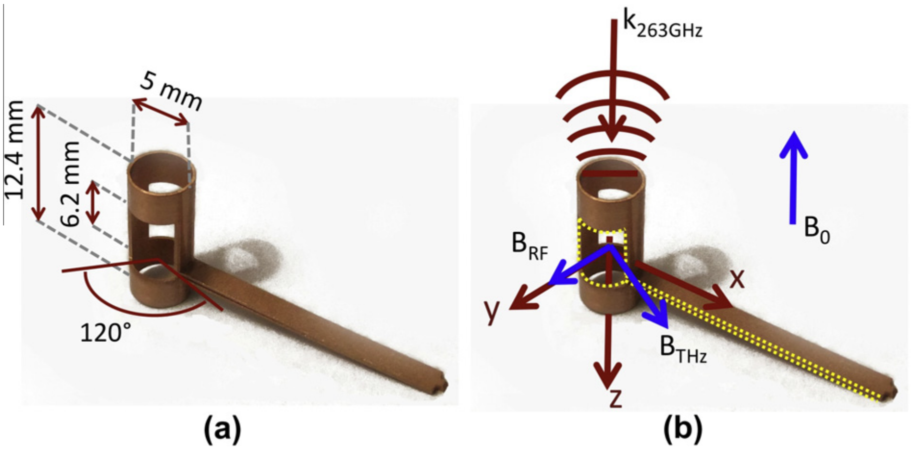

Fig. 1. (a) Picture of the saddle coil with superimposed geometry characteristics. (b) Relative directions of B_{RF}, and B_0 with respect of the saddle coil geometry. B_{THz}, useful for DNP purpose, is in the XY-plane. The Cartesian frame of reference is chosen with Z-axis along B_0 = 9.4 T, the origin at mid height of the coil windows, and X-axis is taken along the coil connection.

geometry is a rescaled version of the one described in Ref. [26] to fit standard NMR sample holders with 5 mm outer diameter.

The B_{RF} magnetic field homogeneity inside the sample volume can be determined performing nutation experiments where the NMR signal amplitude is compared after a $\frac{\pi}{2}$ and after a considerably longer excitation pulse, usually a $\frac{9\pi}{2}$ pulse. On the other hand, as for the present work, the homogeneity can be directly calculated by means of numerical simulations of the RF field distribution over the sample volume.

In order to simulate the current injection as it happens when soldering coaxial cables in real experiments, the simulation imposes an oscillating surface current at 400 MHz in the first 0.5 mm of the coil's connectors of the saddle coil. The latter was created by a computer-aided design software and exported into *Multiphysics*3.5*a*. Then, we let the current flow and distribute in the coil geometry. A finite conductivity, $\sigma = 5.998 \times 10^7\ \mathrm{Sm}^{-1}$, is associated to the coil geometry corresponding to the copper electric conductivity. The volume where finite-element analysis is performed is surrounded by a perfectly matched layer (PML) that acts as an absorbing boundary for wave equations avoiding any reflection.

In the proposed design, B_{RF} is perpendicular to the axis of symmetry of the tubular region, which is commonly oriented along the direction of the spectrometer magnetic field B_0. The sample volume corresponds to a cylinder of 28 μl with radius in the *XY*-plane of 1.5 mm and height along *Z* of 4 mm. With this choice, the variation of the B_{RF} amplitude results to be less than 10%, implying a ratio $A_{9\pi/2}/A_{\pi/2} = 0.8$ with A_i the signal amplitude of a free induction decay experiment after a pulse imposing a nutation angle *i*. This value is common for commercial NMR probes for liquids [28]. Simulations related to the homogeneity and the intensity of the time RMS magnetic flux density at 400 MHz corresponding to 1 A of applied current with an output impedance of the power supply of 50 Ω are shown in Fig. 2 for the three main sections of the coil. In particular for this simulation line plots along resp., *X*, *Y*, and *Z* of the chosen Cartesian reference frame (see Fig. 1b) are plotted in Fig. 3.

3. First THz-wave results and validation

In order to evaluate the reliability of simulations at 263 GHz, we have done some tests comparing numerical results with measurements performed on an optical table pictured in Fig. 4. The experimental set-up is made up of the saddle coil shined upon by a THz-wave linearly polarized Gaussian beam propagating along *Z*-axis (see Fig. 1b).

In the proposed saddle coil, the THz-wave irradiation of the sample can be obtained through a THz beam propagating along the axis of the coil, as shown in Fig. 1b. As common for quasi-optical propagation at millimeter and sub-millimeter wavelengths, the incoming wave will be assumed as given by a $TEM_{0,0}$ Gaussian beam, which represents the lowest order mode of a free-space propagation satisfying the paraxial approximation. The complex electric field amplitude of the $TEM_{0,0}$ mode is given by

$$E_{r,z} = E_0 \frac{w_0}{w(z)} exp\left(\frac{-r^2}{w^2(z)}\right) exp\left(-ikz - ik\frac{r^2}{R(z)}\right) \tag{3}$$

where *r* is the radial distance from the center axis of the beam, *z* the axial distance from the beam's narrowest point called "waist", *k* is the wave number, $w(z)$ is the radius at which the field amplitude drop to $1/e$ of its axial value, $w_0 = w(0)$ is the waist size, $R(z)$ is the radius of curvature of the beam wavefront. In the proposed configuration, the roughly cylindrical geometry of the coil conforms to the cylindrical symmetry of the incoming beam, whose propagation direction is coaxial to the coil, as indicated in Fig. 1b. The distortion of the free space THz-wave due to the finite size of the coil can be limited by focusing the beam, at least in the cases in which the diameter of the coil is considerably higher than the beam waist.

The THz-wave propagation along the saddle coil has been experimentally investigated by means of the setup shown in Fig. 4. Here, the linearly polarized radiation emitted by a solid state source (Virginia Diodes Inc.) is focused with a plane phase front onto the entrance of the coil by means of a dielectric lens, which allows a control over the characteristics and the purity of the mode. After the propagation in the coil region, a small portion of the THz-wave with defined linear polarization is collected by means of a fundamental mode TE_{10} rectangular waveguide with cross-section of 0.8 mm × 0.4 mm, which propagates the radiation to a Schottky diode detector. As response to the electromagnetic excitation, the quadratic response of the diode gives a signal proportional to the incident power in the whole range of the investigated conditions. Taking into account the sensitivity of the diode and the power emitted by the source, the THz-wave distribution can be mapped with a dynamic range of about 30 dB and minimum input level of 0.04 μW defined by a Tangential Signal Sensitivity of −44 dBm. This entire receiver device is mounted on an automated XYZ stage piloted by a computer to systematically scan the areas of interest and map the field. The two-dimensional measurements shown in this work represents scans with a sampling step of 0.5 mm on each axis. With respect to the Cartesian reference frame of Fig. 1b, the 2D scans correspond to the *XY*-plane at a distance of 0.1 mm from the exit of the coil. In this investigated configuration, the frequency of the Gaussian beam was fixed at 263 GHz and its polarization orthogonal to the optical bench. The beam waist was $w_0 = 1.67$ mm. Different angular orientations of the saddle coil with respect to the beam polarization have been studied, in particular at 0°, 45°, and 90° with respect to a condition in which the coil connectors are directed along the *X*-axis. Fig. 5a–c shows measurements for these three different positions. The measured linear polarization always coincided with the injected one. The observed

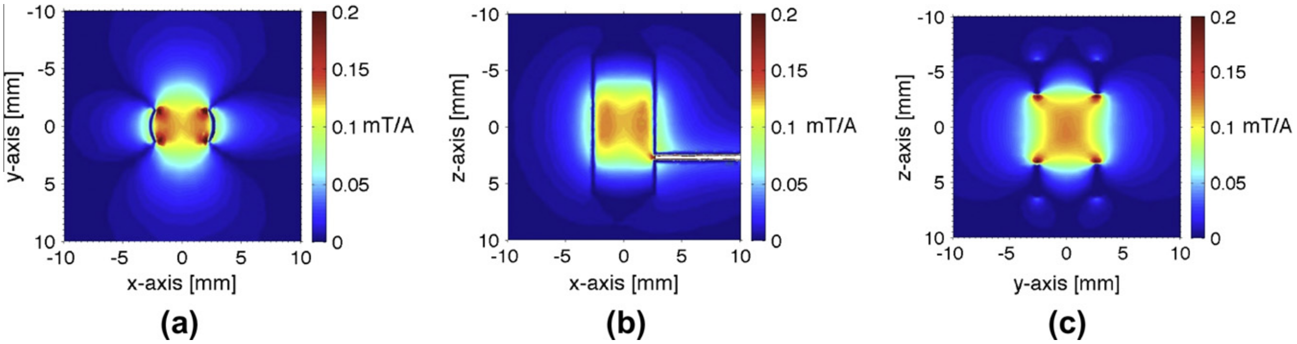

Fig. 2. Saddle coil simulation results of the time RMS magnetic flux density in *y*-direction at 400 MHz. Cross-section plot of the magnetic field strength respectively in the (a) *XY* plane, (b) *XZ* plane, and (c) *YZ* plane.

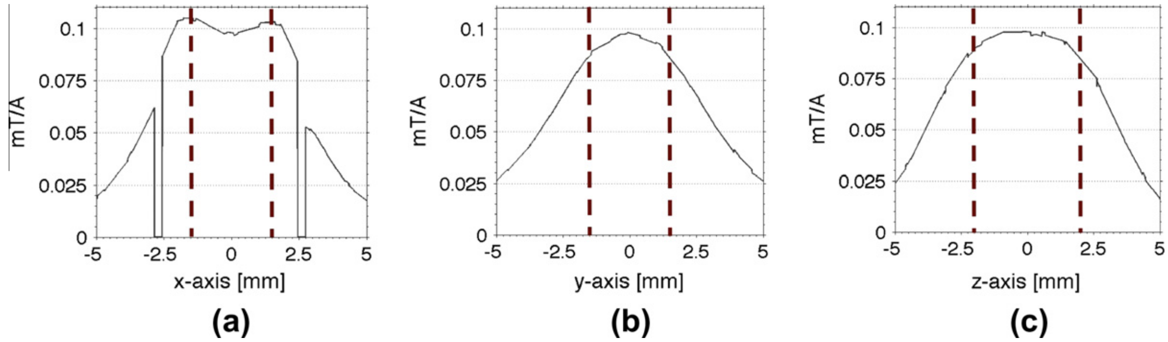

Fig. 3. Line plot of the RMS magnetic flux density at 400 MHz along, respectively (a) *X*-axis, (b) *Y*-axis, and (c) *Z*-axis. In these plots, red dotted lines determine the region where variation from the maximum strength of B_{RF} is less than 10%.

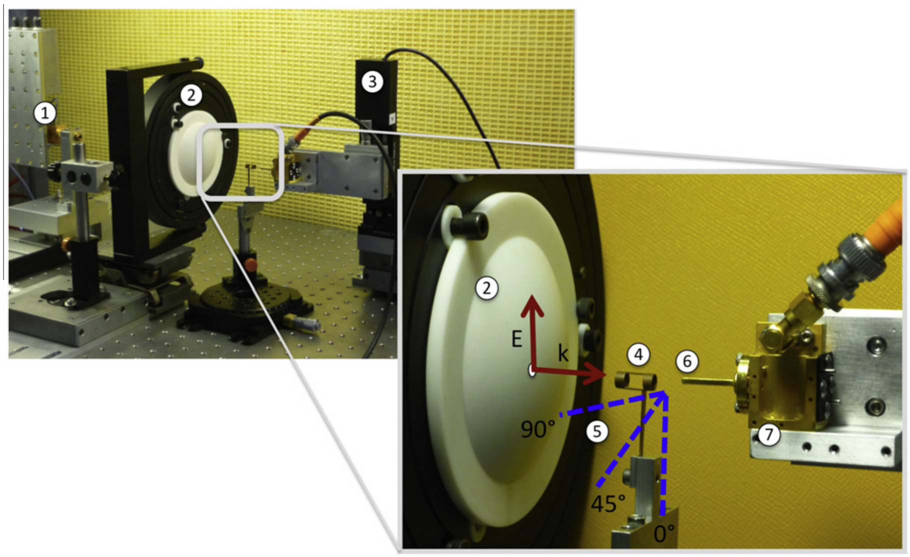

Fig. 4. Optical table set-up for comparison between measurements and simulations shown in this work. The numbering on the figure correspond to: (1) 14 mW, 250–270 GHz, tunable solid state source, (2) dielectric lens for waist size control, (3) *XYZ* motorized stages, 5 cm excursion, 10 μm minimum step, ±2 μm accuracy, superimposed the wave-vector and the direction of the linearly polarized electric field, (4) electro machined saddle coil as represented in Fig. 1, (5) the three explored relative angular orientations of the saddle coil with respect to the Gaussian beam axis of polarization, (6) rectangular waveguide (0.8 mm × 0.4 mm) used to sample the electric field at 263 GHz. With this section only the TE_{01} mode propagates along the 4 cm rectangular waveguide, (7) Schottky diode sensitives, with respect to the picture, to electric field component along the *x*-axis (see Fig. 1b). Microwave absorber have been removed from mounts for illustration clarity.

patterns are very distinctive. Despite the inner diameter of the coil being considerably larger than the beam waist, the initial Gaussian phase front is strongly modified during the propagation along the coil. This is mainly due to the diffraction of the THz-wave beam, which leads to a spatial broadening of the beam, with a consequent reflection on the inner walls of the coil. At the exit of the coil, in particular in the plane on which the beam is mapped, the beam shows pronounced lobes oriented along the direction of the incoming E-field. The presence of characteristic side lobes with very low intensity is a clear indication on the sensitivity of the employed measurement technique. The differences among the power distributions related to the three polarization of Fig. 5a–c evidence that the imperfect cylindrical geometry of the coil, mainly due to its side windows, has a relevant influence on the THz-wave propagation. In particular, it influences the distribution of the incoming power between the main lobes and the secondary ones.

In parallel to the measurements, simulations have been run to reproduce the same experimental conditions. The geometry of the coil was directly imported in the simulation program from computer assisted design software such as *Solidworks* (Dassault Systèmes Corp.), used both to design and control the EDM process. The region of space involved in the simulation was delimited by a cylinder surrounding the coil geometry. Moreover a perfectly matched layer assures that no reflections arise from simulation bounds. At the entrance of the coil, a Gaussian beam with the same beam waist as the experimental configuration has been imposed. The body of the coil was considered as a perfect conductor. Fig. 6 shows the typical field distributions in the investigated volume, both in the case of empty volume (Fig. 6a) and in the case of the coil (Fig. 6). With respect to the free-space propagation, the coil introduces standing waves in the propagation patterns, due to the sharp variations in the geometry of the coil along the propagation direction, as well as a kind of periodic refocusing of the wave, generated by the conducting walls of the coil, as anticipated. The calculated distribution of the electromagnetic wave in the *XY* plane of scanning is reported in Fig. 5d–n for the various investigated polarizations. In particular, Fig. 5d–f shows the total time averaged *z*-component of the Poynting vector, as calculated by

$$\langle(\mathbf{E}\times\mathbf{H})_z\rangle_t = \frac{1}{2\mu_0}\Re\left(E_x B_y^* - E_y B_x^*\right), \tag{4}$$

where $\Re$ indicates the real part of the variables and the star indicates the complex conjugate. Since the setup employed to map the electromagnetic field distribution is selective in the polarization

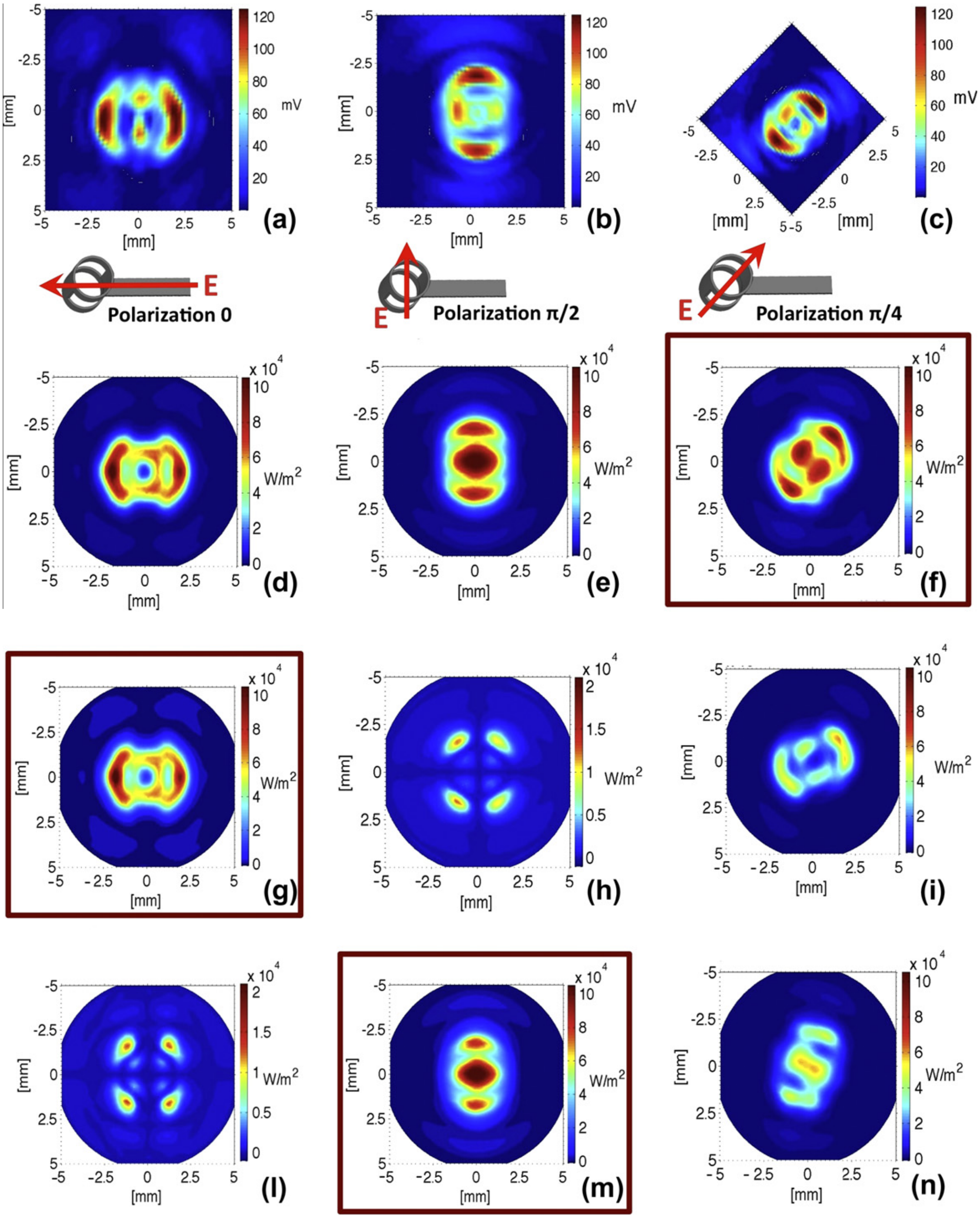

Fig. 5. Comparison between measurements, (a–c), and simulations at 263 GHz for the experimental configuration shown in Fig. 4 with the injected E-field linearly polarized resp., along *X*-axis, *Y*-axis and at 45°. From simulations, the *z*-component of the time averaged Poynting vector, $\langle(\mathbf{E}\times\mathbf{H})_z\rangle_t$, is shown in (d–f) resp., for the three different polarizations. The part of the *z*-component of the Poynting vector related resp. to E_x, $\langle(\mathbf{E}\times\mathbf{H})_z\rangle_{t,x}$, and E_y, $\langle(\mathbf{E}\times\mathbf{H})_z\rangle_{t,y}$ are isolated in plots resp., (g–i) and (l–n). Measurements are in correspondence with simulations, as highlighted by red continuos lines for each column.

of the wave, it probes separately the energy flux in the *z* direction coming from fields having orthogonal polarization, as given for instance by the pairs (Ex, By) and (Ey, Bx). Accordingly, for each of the three investigated polarizations we plotted in Fig. 5g–i the component of the calculated Pointing vector related to the fields polarized along the x direction, given by:

$$\langle(\mathbf{E}\times\mathbf{H})_z\rangle_{t,x} = \frac{1}{2\mu_0}\Re\left(E_x B_y^*\right) \tag{5}$$

and in Fig. 5l–n the component related to the *y*-direction:

$$\langle(\mathbf{E}\times\mathbf{H})_z\rangle_{t,y} = -\frac{1}{2\mu_0}\Re\left(E_y B_x^*\right) \tag{6}$$

Remembering that in the measurements, the polarization of the mode propagating along the fundamental mode TE_{10} rectangular waveguide was parallel to the polarization of the incoming wave, the correspondence between measured and calculated electromagnetic patterns can be established as shown by the red boxes in Fig. 5. It has to be noticed how the orientation of the more intense pattern, mainly depicted with hot colors, is in excellent agreement

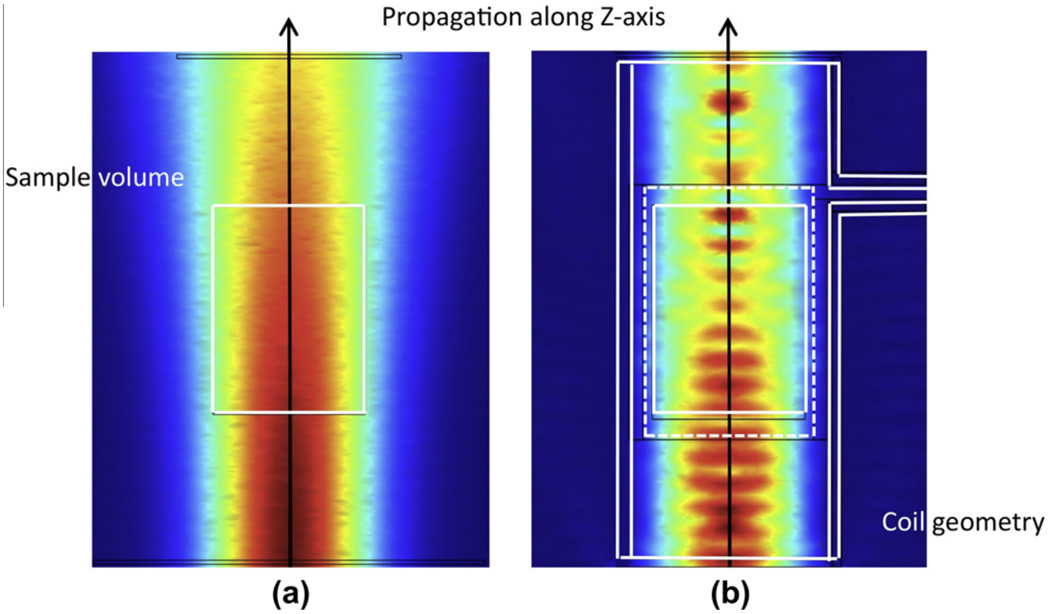

Fig. 6. *XY*-components of the time RMS magnetic field in the *XZ*-plane section for a gaussian beam at 263 GHz propagating along *z*-axis with w_0 = 1.67 mm at the coil entrance in: (a) free-space, and (b) in presence of the proposed saddle coil geometry. The linear color scales have both been normalized and sample volume emphasized.

with simulations. Moreover for the case related to polarization at 45°, where the measurement picks the projection of both E_x and E_y, the similarities between simulation and measurements are indubitable. In addition less intense side lobes are in good correspondence as for instance when looking at the lobes observed in the corners in Fig. 5a and g. The main differences between measurements and simulation probably come from the mismatch between the free space mode and the TE_{10} mode at the entrance of the waveguide, which varies from point to point, due to the local direction of propagation of the wave and the local ratio between the electric and magnetic fields. Other differences can come from a possible imperfect alignment between the source and the coil and from its slight deformation due to manipulation during the different tests. Another source of differences is the finite resolution of the sensitive window of the mapping system, although this is probably not relevant in our case, due to the large size of the beam phase front with respect to the wavelength. Despite these limitations, we can however conclude that the agreement between the measured and calculated quantities is very satisfactory, reproducing the main characteristics of the THz–wave beam at the exit of the coil.

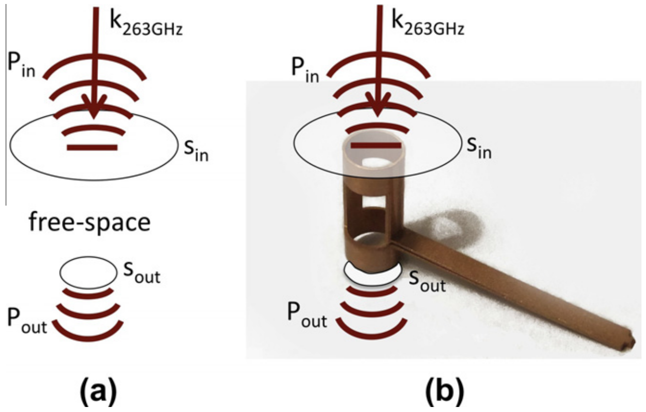

Fig. 7. Pictorial view of a gaussian beam propagating in free-space along an axis parallel to that of the coil (a), and in presence of the saddle coil (b). The two schematic views represent simulated configurations to estimate the power flow ratio passing through two surfaces, s_{in} and s_{out} corresponding resp., at the entrance and the exit of the coil. s_{in} has been chosen to be wide enough to numerically collect mostly all the incident power. The integration surface, s_{out}, has been chosen to quantify the power transmitted trough the coil.

4. THz-wave sample irradiation

The confirmation of the accuracy of the electromagnetic simulations opens the way to a detailed numerical analysis of the electromagnetic field distribution in regions not accessible by the experimental setup and in particular in the sample region inside the saddle coil. To this aim, we have investigated the propagation properties of the coil, considered as an element of the THz-wave circuit as shown in Fig. 7, for configurations relevant for DNP-NMR applications. First, we have considered the THz-wave energy flux along the empty coil, for a variable incoming beam waist. Fig. 8 shows the outgoing power, calculated on the cross section s_{out} at the exit of the coil, over the ingoing power calculated on the cross section s_{in} at the entrance of the coil, with respect to the beam waist.

Since the gaussian beam model (Eq. (3)) uses the paraxial approximation, it fails when wavefronts are tilted by more than about 20° from the direction of propagation [29]. With $\lambda_{263\text{GHz}} = 1.14$ mm and waists typically on the order of $w_0 = 2$ mm the beam divergence defined as:

$$\theta = \frac{\lambda}{\pi w_0} \cong 0.18\ rad \tag{7}$$

is relatively large. In fact, it turns out that the total angular spread of the beam far from the w_0 position, given by 2θ, results to be more than 20°. This becomes evident looking at Fig. 8 where the ratio P_{out}/P_{in} in the simulated case of a gaussian beam in free space, blue[1] line with dots, is compared with the approximated analytical solution shown by dashed line. This evidence stresses again the importance of presented simulations for waist values when analytical approaches can no longer be used.

---

[1] For interpretation of color in Figs. 1–14, the reader is referred to the web version of this article.

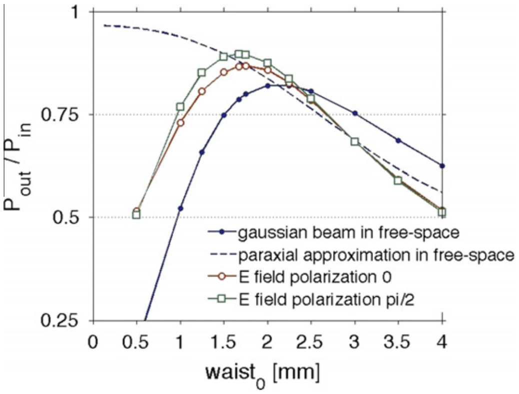

Fig. 8. Results of simulation for the configuration schematized in Fig. 7. The position of the minimum value of the gaussian beam waist, w_0, is chosen to be at the entrance of the saddle coil. By varying, w_0, the ratio P_{out}/P_{in} is plotted in free-space beam propagation and with the coil. For this last configuration two orthogonal polarizations of the magnetic field are shown. Dashed line illustrates the ratio P_{out}/P_{in} in the paraxial approximation for a gaussian beam propagating in free-space.

The ratio P_{out}/P_{in} for incoming waves polarized along X and Y-axis is represented in Fig. 8 by open symbols. The curve referring to the X polarization is quite close to the curve referring to the Y polarization. A further analysis on the polarization of the waves at the exit of the coil confirms, as anticipated by the results of Fig. 5, that the polarization of the wave is preserved along the coil. This property has been verified in the whole range of frequencies accessible with the employed solid-state source, *i.e.* 250–270 GHz.

For a beam waist of 2.5 mm, P_{out}/P_{in} shows the same value for the coil and the free-space propagation. At smaller waists, P_{out}/P_{in} is higher for the coil, since in this cases the guiding effect of the coil overcompensates the diffraction of the beam.

Having established the general conditions in which the available THz-wave power can be efficiently coupled and propagated along the coil, it is necessary to determine the related power-to-magnetic field conversion factor in the sample region, which represents indeed the key electromagnetic quantity in DNP-NMR experiments. In particular, we considered the time root mean square (RMS) of the components of the magnetic field B_{THz} perpendicular to the static field B_0 for unitary incident power averaged in the sample region, V, illustrated in Fig. 9 defined as:

$$B^{*}_{\mathrm{THz}} = \left\langle \frac{1}{V}\int_{V}\sqrt{B^2_{THz,x}+B^2_{THz,y}}\,dV \right\rangle_t \tag{8}$$

A rigorous analysis of this quantity requires the inclusion of the effects of sample and sample holder, whose size is of the order of the employed wavelength.

Figs. 9 and 10 show a possible arrangement for sample and sample holder with respect to the proposed saddle coil. As an illustrative case, the dielectric properties of the sample were assumed coincident with that of a 1M solution of ^{13}C–Urea dissolved in $d_8 - glycerol/\mathrm{D_2O/H_2O}$ (60/30/10% by volume) at 80 K and 263 GHz, as mentioned in Nanni et al. [30]. The sample holder was assumed made of Teflon. The corresponding dielectric properties are $\epsilon' = 3.5$, and $\tan\,\delta = 0.009$ for the sample and $\epsilon' = 2$, $\tan\,\delta = 2.8 \times 10^{-4}$ for the holder where ϵ' is the real part of the dielectric constant and $\tan\,\delta$ is the loss tangent.

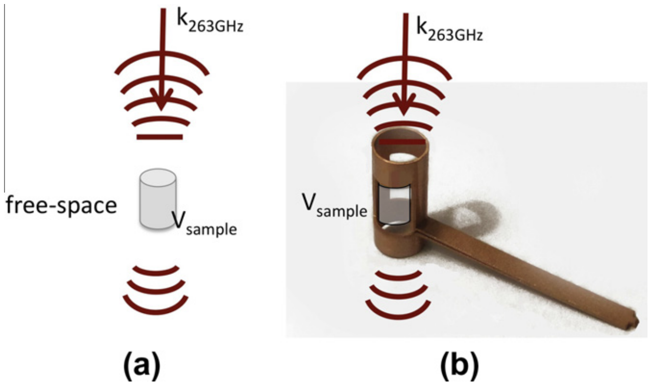

Fig. 9. Pictorial view of a gaussian beam propagating in free-space along an axis parallel to that of the coil (a), and in presence of the saddle coil (b). The two schematic views represent simulated configurations to estimate the RMS magnetic flux density components useful for DNP technique B^{*}_{THz}. This volume corresponds to the region where B_{RF} is considered homogeneous enough, *i.e.* variation of B_{RF} less than 10% (see Fig. 3).

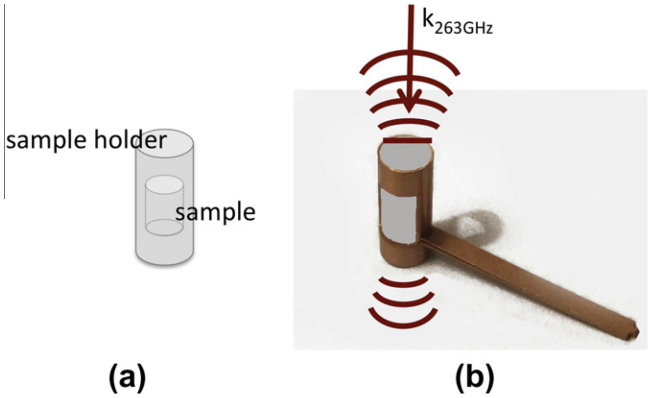

Fig. 10. (a) A sample holder with the shape of a cylinder with diameter and height corresponding to the internal dimension of the saddle coil has been chosen. The sample volume corresponds to the integration region depicted in Fig. 3, *i.e.* variation of B_{RF} less than 10%. Total sample volume corresponds to 28 μl. (b) Simulations have been run on the system composed by the coil, the sample holder and the sample shined upon by a gaussian beam at 263 GHz propagating along z-axis with w_0 at the coil top entrance.

The results of the electromagnetic simulations are shown in Fig. 11, for the same electric field polarizations as Fig. 8. Without any load in the coil, the average magnetic field strength, B^{*}_{THz}, with respect to the beam waist is basically the same for both injected orthogonal polarizations. The obtained values almost correspond to that for the gaussian beam propagating in free-space. From the point of view of the amplitude of B^{*}_{THz}, the optimal beam waist is 1.5 mm.

The electromagnetic response of the coil shows a considerably different behavior when loaded by sample and sample holder. For both the investigated E-field polarizations, as well as in the case of incoming wave with circular polarization, B^{*}_{THz} increases more than 25% with respect to the empty coil, the best results corresponding to smaller beam waists. This increase can be partially explained by taking into account the focusing effect due to the real parts of the dielectric constants chosen for ^{13}C–Urea and teflon.

Moreover, the presence of sample and sample holder has a twofold effect on the electromagnetic propagation of the coil. On one hand, it induces a partial reflection of the incoming wave, with a consequent reduction of the irradiation efficiency of the sample. On the other hand, the higher dielectric permittivity of the sample with respect to the free space decreases the ratio between the electric field E_{THz} and the magnetic field B_{THz}. In the investigated case, the latter dominates over the former.

The above results correspond to an experimental set-up that can be defined as single-pass, in which the fields at 263 GHz remain of traveling-wave nature, considering the reflected wave typically as a minor fraction of the whole power.

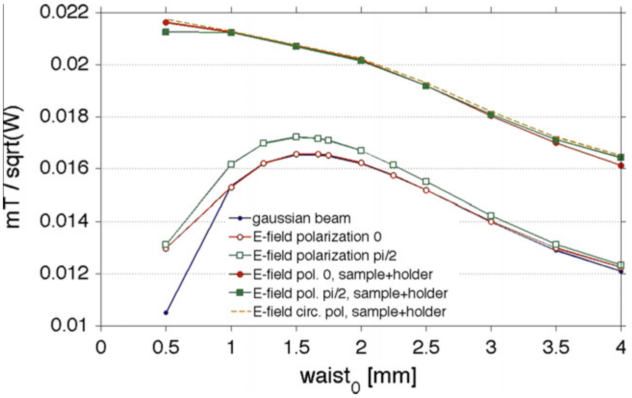

Fig. 11. RMS magnetic flux density in the *XY*-plane averaged in the sample volume for the experimental set-up depicted in Fig. 10a and b. The w_0 of the applied 263.5 GHz gaussian beam at the coil top entrance is varied. In the case of gaussian beam propagating in free-space, the results are represented by the blue line with dots, while in presence of the coil w/o any load for two orthogonal linear polarization along *x*-axis and *y*-axis, results are shown resp. with red line with empty dots and green line with empty squares. In the case of loaded coil (see Fig. 10a and b) dielectric proprieties at 80 K and 263 GHz of Teflon have been chosen for the sample holder: $\epsilon' = 2$, and loss tangent $\tan\delta = 2.8 \times 10^{-4}$. The sample has dielectric proprieties of 1M of ^{13}C–Urea dissolved in $d_8 - glycerol$/D$_2$O/H$_2$O (60/30/10% by volume) at 80 K and 263 GHz as mentioned in Nanni et al. [30]: $\epsilon' = 3.5$, and loss tangent $\tan\delta = 0.009$. In addition of the two orthogonal linear polarization giving very similar results , circular polarization behavior has been checked. Results shown by the dashed orange line confirm that the chosen geometry preserves the incident polarization.

On the other hand, by working with a multiple pass propagation circuit one can achieve stronger THz-wave magnetic fields. Fig. 12a shows the simplest multiple pass circuit, where a metalized surface has been put on the sample holder at the bottom exit of the saddle coil. For the investigated cases, the double passage of the radiation through the sample leads to an increase of almost 25% in the magnetic field B^*_{THz}. In practical DNP-NMR applications, often characterized by very intense THz-wave irradiations, another crucial quantity is given by the electromagnetic energy dissipated in the sample due to its dielectric absorption. For the cases treated in Figs. 12 and 13, the fraction of total incoming power dissipated in the sample is about 40% for the single pass configuration, and about 60% in the double pass configuration, whereas the power dissipated in the sample holder is about 3% in both cases.

Both for the single and double pass configuration, the dielectric properties assumed for the sample lead to a consistent dielectric absorption, which can correspond to a relevant heating of the sample. This is a common problem in the irradiation of samples with sizes comparable or larger than the employed wavelength; it requires a careful control over the irradiation power, especially at low temperatures, where the heat capacities and thermal conductivities usually decrease.

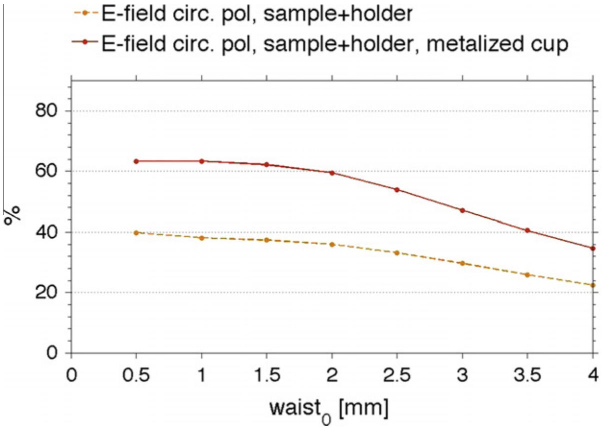

Fig. 13. Dielectric losses in the sample as a percentage of the injected power in the case depicted in Fig. 10b and Fig. 12a for an incident electric field circularly polarized at 263 GHz.

In order to provide a way to mitigate this problem, we numerically explored the response of the DNP-NMR probe in terms of B^*_{THz} and fraction of dissipated power, for different dielectric permittivities of the sample and the sample holder, in the experimental configuration of Fig. 10b. The scanned permittivity range corresponds to the dielectric characteristics of common materials at 263 GHz and few tens of Kelvin, in particular to Sapphire and Zirconium ($\epsilon' \approx 9$) and Quartz ($\epsilon' \approx 4.6$) [31] approximately having the same $\tan\delta = 2.8 \cdot 10^{-4}$ of teflon.

Results are summarized in Fig. 14. In particular, the behavior of B^*_{THz} is shown in Fig. 14a, whereas the behavior of the fraction of power dissipated in the sample in shown in Fig. 14b. By comparing the two graphs it turns that when $\epsilon' = 6$ for both sample and holder we can maximize the ratio between magnetic field strength and sample heating in the investigated range of conditions. With this in mind, some possible experimental strategies are proposed in the next section of the paper.

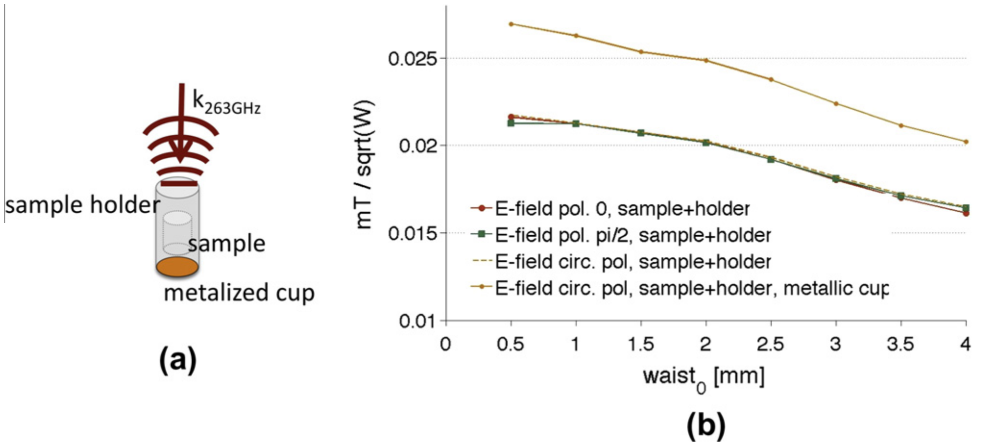

Fig. 12. In presence of the saddle coil, (a) Comparison between the configuration depicted in Fig. 10b and in presence of a metallic surface put on the sample holder at the bottom exit of the coil. (b) Time RMS magnetic flux density in the *XY*-plane averaged in the sample volume, B^*_{THz}, for two orthogonal linear polarization and circular polarization, resp., red, green and orange dashed line, and with metallic cup for circular polarization (orange continuos line).

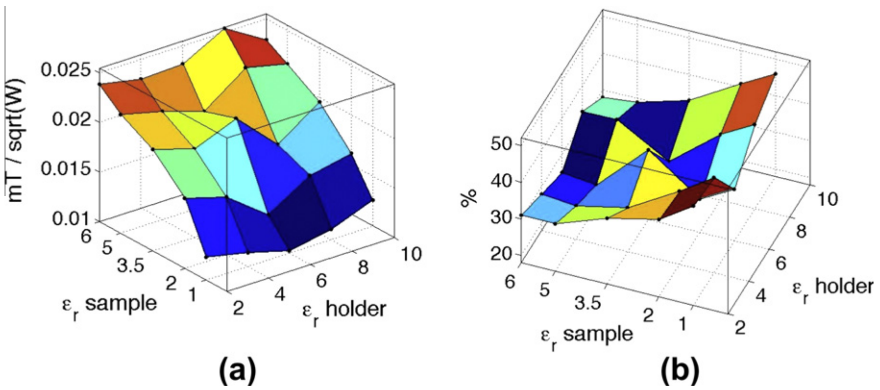

Fig. 14. (a) RMS magnetic flux density in the *XY*-plane averaged in the sample volume, B^{*}_{THz}, for the experimental set-up depicted in Fig. 10a and b for different ϵ' values for the holder and the sample. Conductivity, σ, is unchanged with respect to the previous cases. (b) Sample resistive heating, as a percentage of the injected power, in the same ϵ' ranges.

5. Conclusions and perspectives

A monolithic saddle coil design for DNP-NMR experiments at 9.4 T has been proposed. A characterization of this structure is shown through a finite-element numerical method, both in its radio-frequency (400 MHz) and THz-wave (263 GHz) response.

The numerical results at the radio-frequency were used to determine the relevant sample volume for NMR experiments, preserving the homogeneity of the radio frequency magnetic flux density, leading to a sample volume of 28 μl.

The numerical method for THz simulations has been validated through experiments reproducing the simulated conditions.

Once validated the numerical methods have been used to study extensively the THz wave channeling through the structure, injected into the system along the axis of the saddle coil. The detailed analysis of the THZ wave behavior made it possible to determine the beam parameters needed to optimize the time RMS magnetic flux density useful for DNP experiments and averaged in the sample volume, B^{*}_{THz}. In parallel, the power dissipated through dielectric losses in the system was estimated. The injected gaussian beam showed optimal behavior when injected with a plane phase front and a waist $\omega_0 = 1.5$ mm onto the entrance of the saddle coil.

Two systems have been studied: the first one being composed of the saddle coil, a simple cylindrical geometry for a teflon sample holder as well as a ^{13}C Urea sample, along with their dielectric properties at 80 K and 263 GHz. It is shown that this configuration gives rise to a single pass traveling wave situation, where the relevant field can reach $B^{*}_{\mathrm{THz}} = 0.021\ \mathrm{mT}/\sqrt{\mathrm{W}}$ and about 40% of the injected power is found to be dissipated into the sample. The second configuration is identical to the first one with an additional metalized cup on the bottom exit of the sample holder. It is shown that this configuration gives rise to a double pass situation, where the relevant field can be raised to $B^{*}_{\mathrm{THz}} = 0.026\ \mathrm{mT}/\sqrt{\mathrm{W}}$ with the drawback that the fraction of injected power dissipated into the sample reaches 60%.

It is shown that when channeling THz waves through the structure, the polarization state of the injected beam is conserved, thus pointing to the possibility to channel linearly or circularly polarized THz beams through the sample.

Finally a parametric study of the relevant THz magnetic flux density B^{*}_{THz} as well as the dielectric sample heating is presented as a function of the real part of the sample and the sample holder's dielectric constants, ϵ'. This analysis shows that to reach an optimal B^{*}_{THz} and minimize the dielectric heating of the sample, for both the sample and the sample holder the optimal choice is $\epsilon' = 6$, suggesting the possible dielectric engineering of the system's materials to increase its performances. Such an engineering can for instance be achieved by a wise choice of materials for the sample holder possibly by introducing specific nano-particles to tune the bulk dielectric properties of the sample.

Globally, a monolithic saddle coil for high-field DNP-NMR applications has been designed, built, and systematically characterized by means of experimental and numerical techniques. These latter, based on advanced numerical software and on large computational resources were proven reliable also in very demanding applications involving over-moded structures. Thus, they represent an ideal way for a systematic exploration, design, and optimization of the many devices still needed in the rapidly growing world of the high-field DNP-NMR.

Acknowledgments

The authors would like to thank the precious work of all the EPFL technicians involved in the experimental set-up. In particular, Samuel Allenspach at CRPP and Gilles Grandjean and Olivier Haldimann on behalf of the entire IPMC workshop staff. All shown simulations would not have been possible without the contribution of Tran Trach-Minh. We are also grateful to Giovanni Boero for the constructive discussion. Work supported by Requip (No. 206021-121303/1), Sinergia (No. CRSI20-122708/1) and (no: 200020-120503/1) Grants of the Swiss National Science Foundation and by the Ecole Polytechnique Fédérale de Lausanne.

References

[1] T. Prisner, W. Kockenberger, Dynamic nuclear polarization: new experimental and methodology approaches and applications in physics, chemistry, biology and medicine, Applied Magnetic Resonance 34 (2008) 213–218.

[2] A. Torrezan, S.T. Han, I. Mastovsky, M. Shapiro, J. Sirigiri, R. Temkin, et al., Continuous-wave operation of a frequency-tunable 460-GHz second-harmonic gyrotron for enhanced nuclear magnetic resonance, IEEE Transactions on Plasma Science 38 (6) (2010) 1150–1159, doi:10.1109/TPS.2010.2046617.

[3] V. Denysenkov, M.J. Prandolini, M. Gafurov, D. Sezer, B. Endeward, T.F. Prisner, Liquid state DNP using a 260 GHz high power gyrotron, Physical Chemistry Chemical Physics 12 (2010) 5786–5790, doi:10.1039/C003697H.

[4] M. Rosay, L. Tometich, S. Pawsey, R. Bader, R. Schauwecker, M. Blank, et al., Solid-state dynamic nuclear polarization at 263 GHz: spectrometer design and experimental results, Physical Chemistry Chemical Physics 12 (2010) 5850–5860, doi:10.1039/C003685B.

[5] Y. Matsuki, H. Takahashi, K. Ueda, T. Idehara, I. Ogawa, M. Toda, et al., Dynamic nuclear polarization experiments at 14.1 T for solid-state NMR, Physical Chemistry Chemical Physics 12 (2010) 5799–5803, doi:10.1039/C002268C.

[6] R. Panek, J. Granwehr, J. Leggett, W. Kockenberger, Slice-selective single scan proton cosy with dynamic nuclear polarization, Physical Chemistry Chemical Physics 12 (2010) 5771–5778, doi:10.1039/C002710N.

[7] C. Ludwig, I. Marin-Montesinos, M.G. Saunders, A.H. Emwas, Z. Pikramenou, S.P. Hammond, et al., Application of ex situ dynamic nuclear polarization in studying small molecules, Physical Chemistry Chemical Physics 12 (2010) 5868–5871, doi:10.1039/C002700F.

[8] M.H. Lerche, S. Meier, P.R. Jensen, S.O. Hustvedt, M. Karlsson, J. Duus, et al., Quantitative dynamic nuclear polarization-NMR on blood plasma for assays of drug metabolism, NMR in Biomedicine 24 (1) (2011) 96–103, doi:10.1002/nbm.1561.

[9] J.H. Ardenkjr-Larsen, B. Fridlund, A. Gram, G. Hansson, L. Hansson, M.H. Lerche, et al., Increase in signal-to-noise ratio of >10,000 times in liquid-state NMR, Proceedings of the National Academy of Sciences 100 (18) (2003) 10158–10163, doi:10.1073/pnas.1733835100.

[10] A.W. Overhauser, Polarization of nuclei in metals, Physical Review 92 (2) (1953) 411–415, doi:10.1103/PhysRev.92.411.

[11] T. Carver, C. Slicher, Polarization of nuclei spins in metals, Physical Review 92 (1953) 212.

[12] K.H. Hausser, D. Stehlik, Dynamic nuclear polarization in liquids, Advances in Magnetic Resonance 3 (1968) 79–139.

[13] R. Wind, M. Duijvestijn, C. van der Lugt, A. Manenschijn, J. Vriend, Applications of dynamic nuclear polarization in ^{13}C NMR in solids, Progress in Nuclear Magnetic Resonance Spectroscopy 17 (1985) 33–67.

[14] D. Singel, H.K.R.D. Seidel, C. Yannoni, A spectrometer for EPR, DNP, and multinuclear high-resolution NMR, Journal of Magnetic Resonance (1969) 81 (1) (1989) 145–161.

[15] M. Afeworki, R.A. McKay, J. Schaefer, Selective observation of the interface of heterogeneous polycarbonate/polystyrene blends by dynamic nuclear polarization carbon-13 NMR spectroscopy, Macromolecules 25 (16) (1992) 4084–4091.

[16] A. Henstra, P. Dirksen, W. Wenckebach, Enhanced dynamic nuclear polarization by the integrated solid effect, Physics Letters A 134 (2) (1988) 134–136. Cited By (since 1996) 20.

[17] L.R. Becerra, G.J. Gerfen, R.J. Temkin, D.J. Singel, R.G. Griffin, Dynamic nuclear polarization with a cyclotron resonance maser at 5 T, Physical Review Letters 71 (1993) 3561.

[18] A.B. Barnes, G. De Pape, P.C.A. van der Wel, K.N. Hu, C.G. Joo, V.S. Bajaj, et al., High-field dynamic nuclear polarization for solid and solution biological NMR, Applied Magnetic Resonance 34 (2008) 237–263.

[19] V. Vitzthum, M.A. Caporini, G. Bodenhausen, Solid-state nitrogen-14 nuclear magnetic resonance enhanced by dynamic nuclear polarization using a gyrotron, Journal of Magnetic Resonance 205 (1) (2010) 177–179, doi:10.1016/j.jmr.2010.04.014.

[20] J. Mispelter, M. Lupu, Homogeneous resonators for magnetic resonance: a review, Comptes Rendus Chimie 11 (4–5) (2008) 340–355.

[21] L.R. Becerra, G.J. Gerfen, B.F. Bellew, J.A. Bryant, D.A. Hall, S.J. Inati, et al., A spectrometer for dynamic nuclear polarization and electron paramagnetic resonance at high frequencies, Journal of Magnetic Resonance, Series A 117 (1) (1995) 28–40, doi:10.1006/jmra.1995.9975.

[22] M. Bennati, C. Luchinat, G. Parigi, M.T. Trke, Water 1 h relaxation dispersion analysis on a nitroxide radical provides information on the maximal signal enhancement in overhauser dynamic nuclear polarization experiments, Physical Chemistry Chemical Physics 12 (22) (2010) 5902–5910.

[23] E. Kryukov, M. Newton, K. Pike, D. Bolton, R. Kowalczyk, A. Howes, et al., DNP enhanced NMR using a high-power 94 GHz microwave source: a study of the tempol radical in toluene, Physical Chemistry Chemical Physics 12 (22) (2010) 5757–5765.

[24] E. de Rijk, Millimeter waves for signal enhancement in Nuclear Magnetic Resonance, master's thesis, University of Amsterdam, 2010.

[25] B.D. Armstrong, D.T. Edwards, R.J. Wylde, S.A. Walker, S. Han, A 200 GHz dynamic nuclear polarization spectrometer, Physical Chemistry Chemical Physics 12 (2010) 5920–5926.

[26] L.F. Fuks, F.S.C. Huang, C.M. Carter, W.A. Edelstein, P.B. Roemer, Susceptibility, lineshape, and shimming in high-resolution NMR, Journal of Magnetic Resonance (1969) 100 (2) (1992) 229–242.

[27] F. Bonetto, E. Anoardo, M. Polello, Saddle coils for uniform static magnetic field generation in NMR experiments: concepts in magnetic resonance, Part B: Magnetic Resonance Engineering 29B (2) (2006) 9–19.

[28] J. Bart, J. Janssen, P. van Bentum, A. Kentgens, J. Gardeniers, Optimization of stripline-based microfluidic chips for high-resolution NMR, Journal of Magnetic Resonance 201 (2) (2009) 175–185.

[29] A.E. Siegman, Lasers, University Science Books, 1986.

[30] E. Nanni, A. Barnes, Y. Matsuki, P. Woskov, B. Corzilius, R. Griffin, et al., Optimization of thz wave coupling into samples in DNP/NMR spectroscopy, in: Infrared millimeter and terahertz waves (IRMMW-THz), 2010 35th international conference, 2010, pp. 1–3, doi:doi:10.1109/ICIMW.2010.5612956.

[31] J.W. Lamb, Miscellaneous data on materials for millimetre and submillimetre optics, International Journal of Infrared and Millimeter Waves 17 (1996) 1997–2034.